nature

https://doi.org/10.1038/s41586-023-06363-3

Accelerated Article Preview

Quantum metric-induced nonlinear transport in a topological antiferromagnet

Received: 16 January 2023

Accepted: 22 June 2023

Accelerated Article Preview

Cite this article as: Wang, N. et al. Quantum metric-induced nonlinear transport in a topological antiferromagnet. *Nature* https://doi.org/10.1038/s41586-023-06363-3 (2023)

Naizhou Wang, Daniel Kaplan, Zhaowei Zhang, Tobias Holder, Ning Cao, Aifeng Wang, Xiaoyuan Zhou, Feifei Zhou, Zhengzhi Jiang, Chusheng Zhang, Shihao Ru, Hongbing Cai, Kenji Watanabe, Takashi Taniguchi, Binghai Yan & Weibo Gao

Title: Quantum metric-induced nonlinear transport in a topological antiferromagnet

Authors: Naizhou Wang[1], Daniel Kaplan[2], Zhaowei Zhang[1], Tobias Holder[2], Ning Cao[3], Aifeng Wang[3], Xiaoyuan Zhou[3], Feifei Zhou[1], Zhengzhi Jiang[1], Chusheng Zhang[1], Shihao Ru[1], Hongbing Cai[1], Kenji Watanabe[4], Takashi Taniguchi[5], Binghai Yan[2]*, Weibo Gao[1]*

[1] Division of Physics and Applied Physics, School of Physical and Mathematical Sciences, Nanyang Technological University, Singapore, Singapore

[2] Department of Condensed Matter Physics, Weizmann Institute of Science, Rehovot, Israel

[3] Low Temperature Physics Laboratory, College of Physics and Center for Quantum Materials and Devices, Chongqing University, Chongqing, China

[4] Research Center for Functional Materials, National Institute for Materials Science, 1-1 Namiki, Tsukuba, Japan

[5] International Center for Materials Nanoarchitectonics, National Institute for Materials Science, 1-1 Namiki, Tsukuba, Japan

*Corresponding authors' email: binghai.yan@weizmann.ac.il; wbgao@ntu.edu.sg

Abstract: The Berry curvature and quantum metric are the imaginary part and real part, respectively, of the quantum geometric tensor which characterizes the topology of quantum states[1]. The former is known to generate a zoo of important discoveries such as quantum Hall effect and anomalous Hall effect (AHE)[2,3], while the consequences of the quantum metric have rarely been probed by transport. Here we report the observation of quantum metric-induced nonlinear transport, including both nonlinear AHE and diode-like nonreciprocal longitudinal response, in thin films of a topological antiferromagnet, $MnBi_2Te_4$. Our observation reveals that the transverse and longitudinal nonlinear conductivities reverse signs when reversing the antiferromagnetic order, diminish above the Néel temperature, and are insensitive to disorder scattering, thus verifying their origin in the band structure topology. They also flip signs between electron and hole-doped regions, in agreement with theoretical calculations. Our work provides a pathway to probe the quantum metric through nonlinear transport and to design magnetic nonlinear devices.

Main text:

Nonlinear transport provides a powerful tool for probing topological physics in solids[4-21]. A prime example of this is the nonlinear anomalous Hall effect (NLAHE) which reveals the Berry curvature dipole on the Fermi surface and has recently been observed in nonmagnetic topological semimetals (as shown in Fig. 1a)[6,9,10,12,14,15]. This provides a powerful means of investigating quantum geometry in flat space. Another NLAHE caused by the quantum metric, the counterpart of the Berry curvature in the quantum geometry, was also predicted for magnetic topological materials, but is yet to be realized in experiments[1,22-30]. The quantum metric measures the amplitude distance between two neighboring Bloch states and determines the electronic properties of a crystal. A very recent theory[26,30] finds that the quantum metric actually gives rise to both NLAHE and the nonreciprocal longitudinal response, the latter of which is characterized by a diode-like longitudinal resistance, in inversion-breaking magnetic materials (as shown in Fig. 1b)[7]. The asymmetric quantum metric (quantum metric dipole) will induce an anomalous motion of the wave packet and generate nonlinear responses in both the longitudinal and transverse directions. Since the quantum metric is antisymmetric under momentum inversion ($k \rightarrow -k$), both time reversal symmetry (T) and inversion symmetry (P) must be broken in order to generate a net quantum metric dipole. Additionally, the combined symmetry PT can exclude the contribution from the Berry curvature dipole[4]. As a result, a system which breaks both P and T but preserves PT is expected to be an ideal platform for studying the quantum metric effect (see supplementary information S1 for detailed symmetry analysis).

After careful consideration, we chose $MnBi_2Te_4$ as the candidate platform to investigate the quantum metric. Compared to the magnetic doped topological insulator, the intrinsic magnetic topological insulator, $MnBi_2Te_4$, gained a lot of interest recently due to its unique properties[17,31-41]. As shown in Fig. 1c and e, the crystal structure of $MnBi_2Te_4$ consists of alternating layers of Te-Bi-Te-Mn-Te-Bi-Te, known as septuple layers (SLs)[33,34]. $MnBi_2Te_4$ has an A-type antiferromagnetic (AFM) ground state, in which the Mn spins in each SL are aligned ferromagnetically with an out-of-plane easy axis but are coupled antiparallel to adjacent SLs. For even-layer $MnBi_2Te_4$, both P and T symmetry are broken but the combined

PT symmetry is preserved below the Néel temperature[37]. Fig. 1d shows the spatial reflectance magnetic circular dichroism (RMCD) mapping of 3SL and 4SL $MnBi_2Te_4$ measured at zero magnetic field, indicating fully compensated AFM states in even layer $MnBi_2Te_4$[40]. In addition, $MnBi_2Te_4$ possesses three-fold rotational symmetry (from the optical second harmonic generation shown in Fig. 1f), which suppresses the Berry curvature dipole even in the absence of *PT*-symmetry, making the contribution from the quantum metric much easier to observe[30,41].

Electron nonlinearity from spin order

To investigate the electron nonlinearity, we fabricated several high-quality, dual gated even-layer $MnBi_2Te_4$ devices. Here, we focus on a 4SL-$MnBi_2Te_4$ device, the schematic structure of which is shown in Fig. 2a. The dual-gate structure allows us to independently control the carrier density and vertical displacement field. As per theoretical predictions, the quantum metric gives rise to both NLAHE and the nonreciprocal longitudinal response[30]. The former is directly measurable via an alternating current (AC) method, while the latter exhibits diode-like nonreciprocal resistance behavior, expressed as: $V_x = R_0(I + \gamma I^2)$ where I represents the applied current, R_0 is the linear resistance, and γ denotes the coefficient characterizing the nonreciprocity[7]. Considering that the nonreciprocal longitudinal response stems from the quadratic term of the current, we adopted the AC method to measure the second-harmonic voltage $V_x^{2\omega}$ to reflect the non-reciprocal behavior in longitudinal direction, which offers a better signal-to-noise ratio (see supplementary information section S4). To measure the linear and non-linear responses of the device, we employed a standard lock-in technique. As depicted in Fig. 2a, an AC current with frequency of ω (I^{ω}) was injected, and the linear voltage V^{ω} and second-harmonic voltage $V^{2\omega}$ are simultaneously probed. In our experiment, the *x*-axis is defined as the current direction and the *y*-axis as the transverse direction to the current. All the measurements are conducted at T = 1.8 K in the absence of a magnetic field unless otherwise specified. Fig. 2b shows the linear longitudinal (V_x^{ω}) and transverse (V_y^{ω}) voltages, indicating good ohmic contact and a negligible misalignment in the Hall bar geometry from the vanishing of V_y^{ω}.

Next, we focus on the nonlinear responses of 4SL-$MnBi_2Te_4$ in opposite AFM states. Utilizing a method akin to those reported previously for

controlling AFM states in CrI_3 or even-layer $MnBi_2Te_4$, we prepared the AFM-I and AFM-II states[37,42] with opposite Néel orders. As shown in Fig. 2c and 2e, the AFM-I state is prepared by sweeping the magnetic field from –7 T to zero, while the AFM-II state is achieved by sweeping the magnetic field from +7 T to zero. For the linear responses, both AFM states exhibited identical longitudinal (V_x^{ω}) voltages, and the transverse (V_y^{ω}) voltages remained at zero (Extended Data Fig. 1). This observation aligns with the fully compensated AFM orders in 4SL-$MnBi_2Te_4$ (Extended Data Fig. 2). However, the nonlinear responses differ significantly from their linear counterparts. Focusing first on the AFM-I state, Fig. 2c shows that while the linear transverse (V_y^{ω}) voltage remains at zero, there is a significant negative nonlinear transverse voltage (notated as $V_y^{2\omega}$) that scales quadratically with the injected current I^{ω}. More importantly, we also detected a prominent negative nonlinear longitudinal voltage (denoted as $V_x^{2\omega}$), with the same order of magnitude as $V_y^{2\omega}$. This observation aligns with the prediction that the quantum metric dipole can induce both nonlinear Hall and nonreciprocal longitudinal response, distinctly different from the response observed in the nonlinear Hall effect caused by the Berry curvature dipole, where only a Hall response is allowed and the longitudinal response is absent[9,10]. The nonreciprocal longitudinal response in $MnBi_2Te_4$ can also be observed through DC measurements (see supplementary information section S4). Subsequently, we prepared the AFM-II state. As shown in Fig. 2d, in sharp contrast, although the amplitudes of $V_y^{2\omega}$ and $V_x^{2\omega}$ remain nearly the same with the AFM-I state, the sign of both flips to positive. The sign reversal of the nonlinear response suggests that the nonlinear response observed in $MnBi_2Te_4$ is associated with the AFM order. We carefully examined and ruled out potential alternative origins, such as thermal effect or accidental diode junction that could lead to a nonlinear effect. We also exclude the possibility that the nonlinear response observed in even-layer $MnBi_2Te_4$ is originated from the residual magnetization (See supplementary information section S2). To further confirm that the nonlinear signal is an intrinsic response originating from the *PT*-symmetric AFM order, we investigate whether the nonlinear response complies with the rotational symmetry of AFM even-layer $MnBi_2Te_4$, where $\sigma_{yxx} = -\sigma_{yyy}$ and $\sigma_{xyy} = -\sigma_{xxx}$. When y aligns with the in-plane crystal axis, it should

follow that $\sigma_{xyy} = -\sigma_{xxx} = 0$. The coexistence of $\sigma_{yxx}^{2\omega}$ and $\sigma_{xxx}^{2\omega}$ in this 4SL-$MnBi_2Te_4$ device suggests some misalignment between *x/y* and the crystal axes, consistent with our optical SHG measurement in Fig. 1f. To substantiate this further, we fabricated another 4SL-$MnBi_2Te_4$ device with radially distributed electrodes aligned to the crystalline axis (dashed line in Fig. 2e). Fig. 2f demonstrates the nonlinear transverse and longitudinal response upon rotation of the current injection direction. Both transverse $V_y^{2\omega}$ and longitudinal $V_x^{2\omega}$ exhibit three-fold symmetry. These observed features align consistently with the symmetry of the AFM even-layer $MnBi_2Te_4$.

We further investigated the temperature dependence of the nonlinear response in $MnBi_2Te_4$. Fig 3a and 3b shows the temperature dependent nonlinear voltages $V_y^{2\omega}$ and $V_x^{2\omega}$ which are prepared at AFM-I and AFM-II states, respectively. As the temperature increases, we found that the nonlinear voltage gradually decreases and vanishes above the Néel temperature of $MnBi_2Te_4$, indicating that the nonlinear response is absent in the non-magnetic states. In addition, the nonlinear response in even-layer $MnBi_2Te_4$ is only presented at the AFM states and vanishes when all spins are aligned in one direction (see details in supplementary information section S3). In summary, we can conclude that the nonlinear response observed is associated with the nonlinearity of electron motion originating from the AFM order in 4SL-$MnBi_2Te_4$.

Quantum metric induced nonlinear transport

We now systematically investigate the microscopic origin of the nonlinear response observed in 4SL-$MnBi_2Te_4$. To quantify the strength of the nonlinear response, we use the nonlinear conductivity, as it is independent of the sample size. In our experiment, we can extract the longitudinal and transverse nonlinear conductivity from our data as $\sigma_{xxx}^{2\omega} = \frac{J_x^{2\omega}}{(E_{xx}^{\omega})^2} = \frac{V_x^{2\omega}}{(I_x^{\omega})^2 R_{xx}^3}\frac{L}{}$ and $\sigma_{yxx}^{2\omega} = \frac{J_y^{2\omega}}{(E_{xx}^{\omega})^2} = \frac{V_y^{2\omega}}{(I_x^{\omega})^2 R_{xx}^3}\frac{L^3}{W^2}$, respectively, where *L* and *W* are the longitudinal and transverse length of the Hall bar device. In theory, the nonlinear conductivity due to an applied electric field E_x in a metal includes three contributions[30],

$$J_c = \sigma_{cxx} E_x^2 = (\sigma_{cxx}^2 + \sigma_{cxx}^1 + \sigma_{cxx}^0) E_x^2 \qquad \text{(Eq. 1)}$$

where σ_{cxx}^{i} has the *i*-th order of τ dependence (*c* = *x* or *y*). Here $\sigma_{cxx}^{2} = -\frac{e^3\tau^2}{\hbar^3}\int d^2k f_n \partial_{k_c}\partial_{k_x}\partial_{k_x}\varepsilon_n(\boldsymbol{k})$ is the nonlinear Drude weight, and $\varepsilon_n(\boldsymbol{k})$ is the energy of Bloch state n at momentum $\boldsymbol{k}$, and f_n is the Fermi Dirac distribution for band *n*. $\sigma_{cxx}^{1} = -\frac{e^3\tau}{\hbar^2}\int d^2k f_n(2\partial_{k_x}\Omega_{\mathrm{n}}^{xc})$, is the Berry curvature dipole contribution[4]. The conductivity due to the normalized dipole of the quantum metric is[30],

$$\sigma_{baa}^{0} = -\frac{e^3}{\hbar^2}\int d^2k f_n(2\partial_{k_b}G_n^{aa} - \partial_{k_a}G_n^{ab}) \qquad \text{(Eq. 2)}$$

Where *a/b* = *x/y*, $G_n^{ab} = \sum_{m\neq n}\frac{A_{nm}^{a}A_{mn}^{b}+A_{nm}^{b}A_{mn}^{a}}{(\varepsilon_n-\varepsilon_m)}$ is the band-energy normalized quantum metric and $\partial_{k_a}G_n^{ab}$ represents the normalized quantum metric dipole. In the specific case of 4SL-$MnBi_2Te_4$, the *PT*-symmetry excludes any contribution from the Berry curvature dipole[4]. Additionally, the Berry curvature dipole contribution, which is even under time-reversal, contradicts the sign reversal of the nonlinear signal between the AFM-I and II phases. It is also worth noting that the skew scattering mechanism can also contribute to the nonlinear response[21,43,44], which is significantly suppressed by *PT*-symmetry[43,45]. Furthermore, we can exclude its contribution based on the scaling analysis discussed subsequently. Therefore, the intrinsic contributions to the nonlinear conductivity in $MnBi_2Te_4$ are determined by the nonlinear Drude weight and the normalized quantum metric dipole.

To verify the dominant contribution from the quantum metric, we investigate the scaling relationship between nonlinear conductivities ($\sigma_{yxx}^{2\omega}$ and $\sigma_{xxx}^{2\omega}$) and the linear conductivity σ_{xx}^{ω} (i.e. scattering time τ) as a function of temperature. Fig. 3c shows the temperature dependence of longitudinal conductivity σ_{xx}^{ω} and charge carrier density n_e. The charge carrier density n_e remains almost unchanged at the temperature of 1.6 to 10 K, suggesting that the τ is the main component to determine the conductivity σ_{xx}^{ω} in this range. By adopting this range, we plot the $\sigma_{yxx}^{2\omega}$ and $\sigma_{xxx}^{2\omega}$ as a function of conductivity σ_{xx}^{ω},

$$\sigma^{2\omega} = \eta_2(\sigma_{xx}^{\omega})^2 + \eta_0 \qquad \text{(Eq. 3)}$$

we find that the predominant contribution to both $\sigma_{xxx}^{2\omega}$ and $\sigma_{yxx}^{2\omega}$ is the intrinsic nonlinear conductivity from the normalized quantum metric

dipole (η_0, τ-independent term). The nonlinear Drude contribution (η_2, τ^2-dependent term) is nearly negligible compared to the intrinsic one, which is reasonable considering the small conductivity and low mobility in $MnBi_2Te_4$. The dominant τ-independent nonlinear conductivity further exclude contribution from the impurity scattering, because its lowest order contribution to the nonlinear conductivity begins at τ^1 (see detailed discussion in supplementary information S7.2) [21,44]. In conclusion, we attribute the nonlinear response observed in 4SL-$MnBi_2Te_4$ to the nonlinear Drude weight and the normalized quantum metric dipole, with the latter being the dominant contributor.

Fermi energy dependent nonlinear response

We next study how the nonlinear conductivity in 4SL-$MnBi_2Te_4$, originating from normalized quantum metric dipole, is influenced by the vertical displacement electric field (denoted as *D*) and the electron charge carrier density (denoted as n_e). We first examine the effect of *D* on the nonlinear response. Although *PT* symmetry is instrumental in isolating the quantum metric dipole contribution, the induced nonlinear response remains even when *PT* is broken by *D*. Furthermore, we note that the Berry curvature dipole induced NLAHE still vanishes because of three-fold rotational symmetry. To demonstrate this, we investigate the dependence of $\sigma_{yxx}^{2\omega}$ on the electric field *D* with fixed carrier density at $n_e \approx -3 \times 10^{12}\ cm^{-2}$. As shown in Fig. 4b, $\sigma_{yxx}^{2\omega}$ changes only slightly when tuning the electric field away from *D*=0. Next, we investigate the effect of charge carrier density *n* on the nonlinear response. Fig. 4c shows the nonlinear conductivity $\sigma_{yxx}^{2\omega}$ and $\sigma_{xxx}^{2\omega}$ as a function of carrier density *n*, respectively. When the Fermi level is tuned into the charge neutral gap, both $\sigma_{yxx}^{2\omega}$ and $\sigma_{xxx}^{2\omega}$ vanish. This is in line with the fact that the quantum metric dipole is a Fermi surface property[30]. Furthermore, both $\sigma_{yxx}^{2\omega}$ and $\sigma_{xxx}^{2\omega}$ exhibit a sign reversal when tuning the carrier density between hole and electron regimes. Lastly, given the evident nonreciprocal longitudinal response, we can evaluate the nonreciprocity coefficient γ in $MnBi_2Te_4$. We find the coefficient γ can reach $\gamma \approx 7 \times 10^{-11} m^2 A^{-1}$, which is two or three orders larger than traditional heavy metal (HM)/ferromagnetic metal (FM) heterostructures (See details in supplementary information section S4.3) [46,47].

To explain our experimental data, we evaluate $\sigma_{yxx}^{2\omega}$ quantitatively by constructing a slab model for 4SL $MnBi_2Te_4$ with density-functional theory (DFT) calculations. Fig. 4d shows the total conductivity as a function of carrier density, in which we assume $\sigma_{yxx}^{2\omega}$ for an ideally aligned device (y aligned with the in-plane crystalline axis). Importantly, around the charge neutrality gap ($\mu = 0$), we observe a sign change which reproduces the experimental findings. (see supplementary information S7.1 for the band-resolved contributions to the quantum metric) The deviation of theoretical $\sigma_{yxx}^{2\omega}$ compared to experimental values may be attributed to the known discrepancy in surface band structure between calculations and experiments on $MnBi_2Te_4$. Additionally, in our calculation, we find that the Drude contribution is small within a large energy range around the Fermi level, indicating that the nonlinear conductivity is primarily driven by the quantum metric dipole. We conducted similar measurements on another 6SL-$MnBi_2Te_4$ device, as detailed in supplementary information section S6.

As a probe, the quantum metric dipole-driven electron nonlinearity in $MnBi_2Te_4$ has several advantages and holds great promise for future applications. First, compared to nonlinearity originating from the Berry curvature dipole or skew scattering, the quantum metric dipole-driven electron nonlinearity is independent of the scattering time, suggesting its robustness against disorder scattering. Second, the quantum metric dipole-driven electron nonlinearity is distinct for opposite AFM spin orders and even robust against small perturbations of external magnetic fields (see details in supplementary information S3), making it a promising candidate for use as a nonlinear magnetic memory device. Finally, the quantum metric dipole-driven nonlinear response is more prominent than the "traditional" nonlinear response from the Berry curvature dipole. We compared the nonlinear response observed in $MnBi_2Te_4$ with other 2D material systems, as presented in Extended Table I. We find that our $MnBi_2Te_4$ devices have a much larger nonlinear conductivity than WTe_2 and strained WSe_2, only smaller than twisted WSe_2 and graphene Moiré superlattices, making $MnBi_2Te_4$ a promising candidate for highly efficient rectifying devices[9,10,13,16,19].

References:

1 Provost, J. P. & Vallee, G. Riemannian structure on manifolds of quantum states. *Commun. Math. Phys.* **76**, 289-301 (1980).

2 Thouless, D. J., Kohmoto, M., Nightingale, M. P. & den Nijs, M. Quantized Hall Conductance in a Two-Dimensional Periodic Potential. *Phys. Rev. Lett.* **49**, 405-408 (1982).

3 Nagaosa, N., Sinova, J., Onoda, S., MacDonald, A. H. & Ong, N. P. Anomalous Hall effect. *Rev. Mod. Phys.* **82**, 1539-1592 (2010).

4 Sodemann, I. & Fu, L. Quantum Nonlinear Hall Effect Induced by Berry Curvature Dipole in Time-Reversal Invariant Materials. *Phys. Rev. Lett.* **115**, 216806 (2015).

5 Ideue, T. *et al.* Bulk rectification effect in a polar semiconductor. *Nat. Phys.* **13**, 578-583 (2017).

6 Du, Z. Z., Wang, C. M., Lu, H. Z. & Xie, X. C. Band Signatures for Strong Nonlinear Hall Effect in Bilayer WTe_2. *Phys. Rev. Lett.* **121**, 266601 (2018).

7 Tokura, Y. & Nagaosa, N. Nonreciprocal responses from non-centrosymmetric quantum materials. *Nat. Commun.* **9**, 3740 (2018).

8 Zhang, Y., Sun, Y. & Yan, B. Berry curvature dipole in Weyl semimetal materials: An ab initio study. *Phys. Rev. B* **97**, 041101 (2018).

9 Kang, K., Li, T., Sohn, E., Shan, J. & Mak, K. F. Nonlinear anomalous Hall effect in few-layer WTe_2. *Nat. Mater.* **18**, 324-328 (2019).

10 Ma, Q. *et al.* Observation of the nonlinear Hall effect under time-reversal-symmetric conditions. *Nature* **565**, 337-342 (2019).

11 Lai, S. *et al.* Third-order nonlinear Hall effect induced by the Berry-connection polarizability tensor. *Nat. Nanotechnol.* **16**, 869-873 (2021).

12 Kumar, D. *et al.* Room-temperature nonlinear Hall effect and wireless radiofrequency rectification in Weyl semimetal $TaIrTe_4$. *Nat. Nanotechnol.* **16**, 421-425 (2021).

13 Qin, M.-S. *et al.* Strain tunable Berry curvature dipole, orbital magnetization and nonlinear Hall effect in WSe_2 monolayer. *Chin. Phys. Lett.* **38**, 017301 (2021).

14 Tiwari, A. *et al.* Giant c-axis nonlinear anomalous Hall effect in Td-$MoTe_2$ and WTe_2. *Nat. Commun.* **12**, 2049 (2021).

15 Du, Z. Z., Lu, H.-Z. & Xie, X. C. Nonlinear Hall effects. *Nat. Rev. Phys.* **3**, 744-752 (2021).
16 He, P. *et al.* Graphene moiré superlattices with giant quantum nonlinearity of chiral Bloch electrons. *Nat. Nanotechnol.* **17**, 378-383 (2022).
17 Zhang, Z. *et al.* Controlled large non-reciprocal charge transport in an intrinsic magnetic topological insulator $MnBi_2Te_4$. *Nat. Commun.* **13**, 6191 (2022).
18 Sinha, S. *et al.* Berry curvature dipole senses topological transition in a moiré superlattice. *Nat. Phys.* **18**, 765-770 (2022).
19 Huang, M. *et al.* Giant nonlinear Hall effect in twisted bilayer WSe_2. *Nat. Sci. Rev.* (2022).
20 Godinho, J. *et al.* Electrically induced and detected Néel vector reversal in a collinear antiferromagnet. *Nat. Commun.* **9**, 4686 (2018).
21 Isobe, H., Xu, S.-Y. & Fu, L. High-frequency rectification via chiral Bloch electrons. *Sci. Adv.* **6**, eaay2497 (2020).
22 Gao, Y., Yang, S. A. & Niu, Q. Field Induced Positional Shift of Bloch Electrons and Its Dynamical Implications. *Phys. Rev. Lett.* **112**, 166601 (2014).
23 Wang, C., Gao, Y. & Xiao, D. Intrinsic Nonlinear Hall Effect in Antiferromagnetic Tetragonal CuMnAs. *Phys. Rev. Lett.* **127**, 277201 (2021).
24 Liu, H. *et al.* Intrinsic Second-Order Anomalous Hall Effect and Its Application in Compensated Antiferromagnets. *Phys. Rev. Lett.* **127**, 277202 (2021).
25 Watanabe, H. & Yanase, Y. Chiral Photocurrent in Parity-Violating Magnet and Enhanced Response in Topological Antiferromagnet. *Phys. Rev. X* **11**, 011001 (2021).
26 Holder, T., Kaplan, D., Ilan, R. & Yan, B. Mixed axial-gravitational anomaly from emergent curved spacetime in nonlinear charge transport. *arXiv:2111.07780* (2021).
27 Lahiri, S., Das, K., Culcer, D. & Agarwal, A. Intrinsic nonlinear conductivity induced by the quantum metric dipole. *arXiv:2207.02178* (2022).

28 Smith, T. B., Pullasseri, L. & Srivastava, A. Momentum-space gravity from the quantum geometry and entropy of Bloch electrons. *Phys. Rev. Res.* **4**, 013217 (2022).

29 Arora, A., Rudner, M. S. & Song, J. C. W. Quantum Plasmonic Nonreciprocity in Parity-Violating Magnets. *Nano Lett.* **22**, 9351-9357 (2022).

30 Kaplan, D., Holder, T. & Yan, B. Unification of Nonlinear Anomalous Hall Effect and Nonreciprocal Magnetoresistance in Metals by the Quantum Geometry. *arXiv:2211.17213* (2022).

31 Chang, C.-Z. *et al.* Experimental Observation of the Quantum Anomalous Hall Effect in a Magnetic Topological Insulator. *Science* **340**, 167-170 (2013).

32 Otrokov, M. M. *et al.* Prediction and observation of an antiferromagnetic topological insulator. *Nature* **576**, 416-422 (2019).

33 Li, J. *et al.* Intrinsic magnetic topological insulators in van der Waals layered $MnBi_2Te_4$-family materials. *Sci. Adv.* **5**, eaaw5685 (2019).

34 Zhang, D. *et al.* Topological Axion States in the Magnetic Insulator $MnBi_2Te_4$ with the Quantized Magnetoelectric Effect. *Phys. Rev. Lett.* **122**, 206401 (2019).

35 Deng, Y. *et al.* Quantum anomalous Hall effect in intrinsic magnetic topological insulator $MnBi_2Te_4$. *Science* **367**, 895-900 (2020).

36 Liu, C. *et al.* Robust axion insulator and Chern insulator phases in a two-dimensional antiferromagnetic topological insulator. *Nat. Mater.* **19**, 522-527 (2020).

37 Gao, A. *et al.* Layer Hall effect in a 2D topological axion antiferromagnet. *Nature* **595**, 521-525 (2021).

38 Deng, H. *et al.* High-temperature quantum anomalous Hall regime in a $MnBi_2Te_4/Bi_2Te_3$ superlattice. *Nat. Phys.* **17**, 36-42 (2021).

39 Cai, J. *et al.* Electric control of a canted-antiferromagnetic Chern insulator. *Nat. Commun.* **13**, 1668 (2022).

40 Yang, S. *et al.* Odd-Even Layer-Number Effect and Layer-Dependent Magnetic Phase Diagrams in $MnBi_2Te_4$. *Phys. Rev. X* **11**, 011003 (2021).

41 Fonseca, J. *et al.* Anomalous Second Harmonic Generation from Atomically Thin $MnBi_2Te_4$. *Nano Lett.* **22**, 10134-10139 (2022).

42 Jiang, S., Shan, J. & Mak, K. F. Electric-field switching of two-dimensional van der Waals magnets. *Nat. Mater.* **17**, 406-410 (2018).

43 Ma, D., Arora, A., Vignale, G. & Song, J. C. Anomalous skew-scattering nonlinear Hall effect in *PT*-symmetric antiferromagnets. *arXiv:2210.14932* (2022).
44 Du, Z. Z., Wang, C. M., Li, S., Lu, H.-Z. & Xie, X. C. Disorder-induced nonlinear Hall effect with time-reversal symmetry. *Nat. Commun.* **10**, 3047 (2019).
45 Watanabe, H. & Yanase, Y. Nonlinear electric transport in odd-parity magnetic multipole systems: Application to Mn-based compounds. *Phys. Rev. Res.* **2**, 043081 (2020).
46 Avci, C. O. *et al.* Unidirectional spin Hall magnetoresistance in ferromagnet/normal metal bilayers. *Nat. Phys.* **11**, 570-575 (2015).
47 Avci, C. O., Mendil, J., Beach, G. S. D. & Gambardella, P. Origins of the Unidirectional Spin Hall Magnetoresistance in Metallic Bilayers. *Phys. Rev. Lett.* **121**, 087207 (2018).

Figure captions:

Figure 1 Quantum metric induced nonlinearity in a *PT*-symmetric AFM. a. The nonlinear Hall effect originating from Berry curvature dipole, which has been observed in systems with broken inversion symmetry. **b.** The nonlinear longitudinal and transverse response observed in a *PT*-symmetric system due to quantum metric dipole. **c.** The crystal structure of even-layer $MnBi_2Te_4$ from the side view. The arrows represent the spin momentum direction of the Mn atoms. **d.** The spatial reflectance magnetic circular dichroism (RMCD) mapping of $MnBi_2Te_4$ measured at zero magnetic field. The dashed line marks the boundary between the 4SL-$MnBi_2Te_4$ and 3SL- $MnBi_2Te_4$. **e.** The crystal structure of $MnBi_2Te_4$ from the top view. The dashed line marked with *M* represents the mirror line. **f.** The angle dependent optical second-harmonic generation (SHG) of the 4SL-$MnBi_2Te_4$ sample. The zero degree corresponds to the applied current direction in the device.

Figure 2 Observation of nonlinear transport in AFM $MnBi_2Te_4$. a. The schematic view of the dual-gated 4SL-layer $MnBi_2Te_4$ device. The linear and nonlinear signals are measured simultaneously with the denoted direction. **b.** The linear longitudinal V_x^{ω} and transverse V_y^{ω} voltage as a function of current I_x^{ω}. The solid line is the linear fitting of the data. **c and d.** The nonlinear longitudinal $V_x^{2\omega}$ and transverse $V_y^{2\omega}$ voltage as a function of current V_x^{ω} for AFM-I and AFM-II states, respectively. At a fixed electric field, the different AFM states are prepared by: AFM-I, sweeping the magnetic field from -7 T to 0 T; AFM-II, sweeping the magnetic field from +7 T to 0 T. The solid lines are quadratic fits to the data. **e.** The optical image of another 4SL-$MnBi_2Te_4$ device with radially distributed electrodes. The dashed line indicates the in-plane crystalline axis, determined by SHG measurement. scale bar: 5 μm. **f.** The nonlinear transverse $V_y^{2\omega}$ and longitudinal $V_x^{2\omega}$ response as a function of current injection angle θ.

Figure 3 Spin order related electron nonlinearity from band-normalized quantum metric dipole. a. Nonlinear transverse voltage $V_y^{2\omega}$ of 4SL-$MnBi_2Te_4$ as a function of temperature for opposite AFM-I and AFM-II states, respectively. The amplitudes of $V_y^{2\omega}$ are similar for the two AFM states but their sign is reversed. $V_y^{2\omega}$ vanishes when the temperature is above the Néel temperature of $MnBi_2Te_4$. **b.** The nonlinear longitudinal voltage $V_x^{2\omega}$ as a function of temperature for opposite AFM-I and AFM-II states, respectively, exhibiting similar trend as $V_y^{2\omega}$. **c.** The conductivity and fitted carrier density of 4SL-$MnBi_2Te_4$ at different temperatures. **d.** The scaling relationship between the nonlinear

conductivity $\sigma_{yxx}^{2\omega}$ ($\sigma_{xxx}^{2\omega}$) and the square of the linear longitudinal conductivity σ_{xx}^{2}. The scaling is carried out at the temperature range of 2 -10 K (marked with shadow area in **c**), in which the carrier density nearly remains constant. The nonlinear transverse and longitudinal conductivities are extracted by $\sigma_{yxx}^{2\omega} = \frac{V_y^{2\omega}}{(I_x^{\omega})^2 R_{xx}^3}\frac{L^3}{W^2}$ and $\sigma_{xxx}^{2\omega} = \frac{V_x^{2\omega}\ L}{(I_x^{\omega})^2 R_{xx}^3}$, respectively. The dashed line is a fit of the data with the scaling relation $\sigma^{2\omega} = \eta_2(\sigma_{xx}^{\omega})^2 + \eta_0$. From the fitting, we conclude that the predominant contribution is from the η_0 term, namely from the intrinsic nonlinear conductivity due to the band-normalized quantum metric dipole.

Figure 4 The electric field and carrier density dependence of the nonlinear response. a. The resistance map of the 4SL-$MnBi_2Te_4$ device. The vertical displacement field *D* and charge carrier density n_e can be independently controlled, as denoted in the figure. **b.** The nonlinear transverse conductivity $\sigma_{yxx}^{2\omega}$ and longitudinal resistance R_{xx} as a function of vertical displacement electric field. The carrier density is fixed at $n_e \approx -3 \times 10^{12}\ cm^{-2}$ as D varies along the dashed line in **a**. **c.** The measured nonlinear transverse conductivity $\sigma_{yxx}^{2\omega}$ and longitudinal conductivity $\sigma_{xxx}^{2\omega}$ as a function of charge carrier density n_e. **d.** The calculated total nonlinear transverse conductivity $\sigma_{yxx}^{2\omega}$ (red line) as a function of carrier density. The grey line denotes the Drude contribution.

Methods

$MnBi_2Te_4$ single Crystal growth

Single crystals of $MnBi_2Te_4$ were grown using a self-flux method[48,49]. The starting materials used in the single crystal processes are Mn slices, Bi lumps, and Te chunks. MnTe and Bi_2Te_3 precursors were prepared by reacting the mixed stoichiometric starting materials at 1100 °C and 900 °C for 24 h, respectively. Then MnTe and Bi_2Te_3 were mixed according to the ratio MnTe: Bi_2Te_3 = 15: 85, loaded into an alumina crucible, and sealed in a quartz tube. The quartz tube was heated to 650 °C in 10 h, dwelled for 12 h, and slowly cooled to 595 °C at a rate of 1 °C/h to grow the single crystals. Shiny single crystals with a typical size of $3\times2\times0.5$ mm^3 can be obtained after centrifuging.

Device fabrication

The $MnBi_2Te_4$ thin flakes were obtained using the Al_2O_3-assisted exfoliation method[35,50]. First, a 70 nm thick layer of Al_2O_3 was thermally evaporated onto bulk $MnBi_2Te_4$ crystals. Second, the Al_2O_3 thin film was lifted along with thin flakes of $MnBi_2Te_4$, which were cleaved from the bulk crystal using thermal release tape. Then, the stacked $MnBi_2Te_4/Al_2O_3$ was transferred onto a transparent Polydimethylsiloxane (PDMS) film. The number of layers in the $MnBi_2Te_4$ thin flakes was determined using optical transmittance measurements. After confirming the layer number, the $MnBi_2Te_4$ thin flake samples were transferred to a Si wafer coated with 285 nm of SiO_2. To ensure high-quality samples, we used a stencil mask method to deposit metal contacts (Cr/Au) on the samples. A 20-40 nm thick h-BN flake was then transferred to the $MnBi_2Te_4$ devices as the top gate dielectric layer, followed by the transfer of a graphite thin flake gate on top of the h-BN/$MnBi_2Te_4$ heterostructure. The entire device fabrication process was carried out in a nitrogen-filled glove box with O_2 and H_2O levels below 1 ppm.

Nonlinear Electrical transport measurements

The electrical transport measurements were performed in a cryogenic-free cryostat equipped with a superconducting magnet (Cryomagnetic). We used a standard lock-in technique (Zurich MFLI) with excitation frequencies ranging from 10 to 200 Hz to measure both the first and second harmonic signals. The data presented in this manuscript was collected at a

low frequency of 17.777 Hz. During the transport measurements, the phase of the first and second harmonic signals was confirmed to be approximately 0 and 90 degrees, respectively (see supplementary information S2.4). The gate voltages were applied using a Keithley 2636 SourceMeter. To independently control the charge carrier density n_e and displacement electric field D, we used a dual gated device structure. The charge carrier density n can be obtained by $n = \left(\frac{\varepsilon_0\varepsilon^{BN}(V_{TG}-V_{TG0})}{d_{BN}} + \varepsilon_0(V_{BG}-V_{BG0})/\left(\frac{d_{Al_2O_3}}{\varepsilon^{Al_2O_3}}+\frac{d_{SiO_2}}{\varepsilon^{SiO_2}}\right)\right)/e$. Here we regarded the Al_2O_3 and SiO_2 dielectric layer as two series connected capacitors. The electric displacement field D can be obtained by $D = \left(\frac{V_{BG}-V_{BG0}}{\left(\frac{d_{Al_2O_3}}{\varepsilon^{Al_2O_3}}+\frac{d_{SiO_2}}{\varepsilon^{SiO_2}}\right)} - \frac{\varepsilon^{BN}(V_{TG}-V_{TG0})}{d_{BN}}\right)/2$. Here, ε_0 is the vacuum permittivity; V_{TG0} and V_{BG0} correspond to the gate voltage of maximum resistance; $\varepsilon^{Al_2O_3}$, ε^{SiO_2} and ε^{BN} are the relative dielectric constant of Al_2O_3, SiO_2 and h-BN; $d_{Al_2O_3}$, d_{SiO_2} and d_{BN} are the thickness of Al_2O_3, SiO_2 and h-BN, respectively. We noticed a minor asymmetry in $\sigma_{yxx}^{2\omega}$ and R_{xx} with respect to the displacement electric field D, possibly attributed to charge trapping induced by substrate effects or disorder[51]. The asymmetry is more pronounced in $\sigma_{yxx}^{2\omega}$, as the quantum metric is related to energy differences between bands and more sensitive to D.

The nonlinear response in the $MnBi_2Te_4$ device with radially distributed devices

For the $MnBi_2Te_4$ device with radially distributed devices, when the current aligns with the in-plane crystal axis ($\theta = 0°$), the transverse $V_y^{2\omega}$ is zero. In contrast, when the current is perpendicular to the crystalline axis ($\theta = 90°$), the longitudinal $V_x^{2\omega}$ is zero. In addition, the nonlinear response should obey the symmetry of even-layer $MnBi_2Te_4$, with $\sigma_{yxx} = -\sigma_{yyy}$ and $\sigma_{xyy} = -\sigma_{xxx}$. To substantiate this, we use the formula for nonlinear conductivity: $\sigma_{xxx}^{2\omega} = \frac{J_x^{2\omega}}{(E_{xx}^{\omega})^2} = \frac{V_x^{2\omega}\ L}{(I_x^{\omega})^2 R_{xx}^3}$ and $\sigma_{yxx}^{2\omega} = \frac{J_y^{2\omega}}{(E_{xx}^{\omega})^2} = \frac{V_y^{2\omega}}{(I_x^{\omega})^2 R_{xx}^3}\frac{L^3}{W^2}$. Here, L refers to the length and W to the width of the device. The optical image (Fig. 2e) reveals that the length-to-width ratio, L/W, is approximately 0.85. Taking into consideration the geometric

characteristics of the device, we conclude that the nonlinear conductivity conforms to $\sigma_{yxx} = -\sigma_{yyy}$ and $\sigma_{xyy} = -\sigma_{xxx}$.

Optical measurement

For the RMCD measurement, a linearly polarized 633 nm HeNe laser was modulated by a photoelastic modulators (PEM) at a frequency of 50 kHz. The laser beam was focused on the sample at normal incidence using an Olympus MPLN50× objective with a 0.75 numerical aperture. The laser spot size was approximately 2 μm, with a power of 1.8 μW. The reflected light was collected by a photodetector and analyzed using a lock-in amplifier set to the same frequency as the PEM. The RMCD measures the differential reflection between left and right circularly polarized light, the magnitude of which is proportional to the magnetic moments of the $MnBi_2Te_4$ sample.

The second harmonic generation (SHG) measurement was performed at room temperature using femtosecond pulse lasers with a central wavelength of 800 nm. The laser beam was focused at normal incidence on the sample using a Nikon ELWD 100x microscope objective. The SHG signals were collected using a spectrometer. To perform the polarization-resolved measurement, a motorized polarizer was used to control the polarization of the incident laser beam as it was rotated next to the objective.

DFT calculations

We use VASP (Vienna ab-initio software package) with the PBE functional in the generalized gradient approximation, to obtain the electronic ground state[52]. We then project the ground state wavefunctions on Wannier functions using Wannier 90[53] and create a tight-binding model with 184 Wannier orbitals. For the Drude contribution we adopt a lifetime of $\tau \approx 40\ fs$ estimated from our experimental conductivity and carrier density in Fig. 2c and theoretical effective mass ($m^* = 0.14m_e$) for the 4 SL film.

Methods references:

48 Cao, N. *et al.* Angle dependent field-driven reorientation transitions in uniaxial antiferromagnet $MnBi_2Te_4$ single crystal. *Appl. Phys. Lett.* **120**, 163102 (2022).

49 Hu, C. *et al.* A van der Waals antiferromagnetic topological insulator with weak interlayer magnetic coupling. *Nat. Commun.* **11**, 97 (2020).
50 Deng, Y. *et al.* Gate-tunable room-temperature ferromagnetism in two-dimensional Fe_3GeTe_2. *Nature* **563**, 94-99 (2018).
51 Fei, Z. *et al.* Ferroelectric switching of a two-dimensional metal. *Nature* **560**, 336-339 (2018).
52 Kresse, G. & Furthmüller, J. Efficient iterative schemes for ab initio total-energy calculations using a plane-wave basis set. *Phys. Rev. B* **54**, 11169-11186 (1996).
53 Mostofi, A. A. *et al.* An updated version of wannier 90: A tool for obtaining maximally-localised Wannier functions. *Comput. Phys. Commun.* **185**, 2309-2310 (2014).

Acknowledgements: We thank Shengyuan A. Yang, Huiying Liu and Suyang Xu for helpful discussion. W.-b.G acknowledges the financial support from the Singapore National Research Foundation through its Competitive Research Program (CRP Award No. NRF-CRP22-2019-0004). B.Y. acknowledges the financial support by the European Research Council (ERC Consolidator Grant No. 815869, "NonlinearTopo") and Israel Science Foundation (ISF No. 2932/21). A. F. Wang acknowledges the financial support from the National Natural Science Foundation of China (Grant No. 12004056), Chongqing Research Program of Basic Research and Frontier Technology, China (Grants No. cstc2021jcyj-msxmX0661) and Fundamental Research Funds for the Central Universities, China (Grant No. 2022CDJXY-002). X.Z acknowledges the financial support from the National Key Research and Development Program of the Ministry of Science and Technology of China (2019YFA0704901) and the National Natural Science Foundation of China (Grant Nos. 52125103, 52071041).

Author contributions: W.-b.G and B.Y conceived and supervised the project. N.W fabricated the devices, performed the transport and RMCD measurement with help from Z.Z and C.Z. D.K, T.H and B.Y performed the theoretical calculations. N.W and F.Z performed the NV measurement with help from Z.J, S.R and H.C. N.W, W.-b.G, D.K, T.H and B.Y analysed the data. N.C, A.W and X.Z grew the $MnBi_2Te_4$ single crystals. K.W and T.T grew the hBN single crystals. N.W, B.Y and W.-b.G wrote the manuscript with input from all authors.

Competing interests: The authors declare no competing interests.

Data availability: Source data in the main text and extended figures are provided with this paper.

Additional information: Correspondence and requests for material should be addressed to Binghai Yan (binghai.yan@weizmann.ac.il) or Wei-bo Gao (wbgao@ntu.edu.sg).

Extended Figure 1 The linear conductivity of 4SL-$MnBi_2Te_4$ with opposite AFM states. a and b. The AFM-I and AFM-II states are prepared by sweeping the magnetic field from -7 T to 0T or +7 T to 0 T, respectively. **c and d.** The linear longitudinal V_x^{ω} and transverse V_y^{ω} voltage as a function of current I_x^{ω} for AFM I and AFM II states, respectively. The solid line is a linear fit to the experimental data.

Extended Figure 2 The fully compensated AFM order in 4SL-$MnBi_2Te_4$ device. A. The magnetic field dependent longitudinal resistance R_{xx} of the 4SL-$MnBi_2Te_4$ device. **B.** The magnetic field dependent Hall resistance R_{yx} of the 4SL-$MnBi_2Te_4$ device. In zero magnetic field, the AFM order is fully compensated and the Hall resistance $R_{yx} = 0$.

Extended Table 1 Comparison of the nonlinear conductivity for $MnBi_2Te_4$ and other two-dimensional material systems. The nonlinear transverse conductivity $\sigma_{yxx}^{2\omega}$ in even-layer $MnBi_2Te_4$ is summarized and compared with other reported material systems[9,10,13,16,19]. The corresponding mechanisms responsible for the nonlinear response are also listed for comparison.

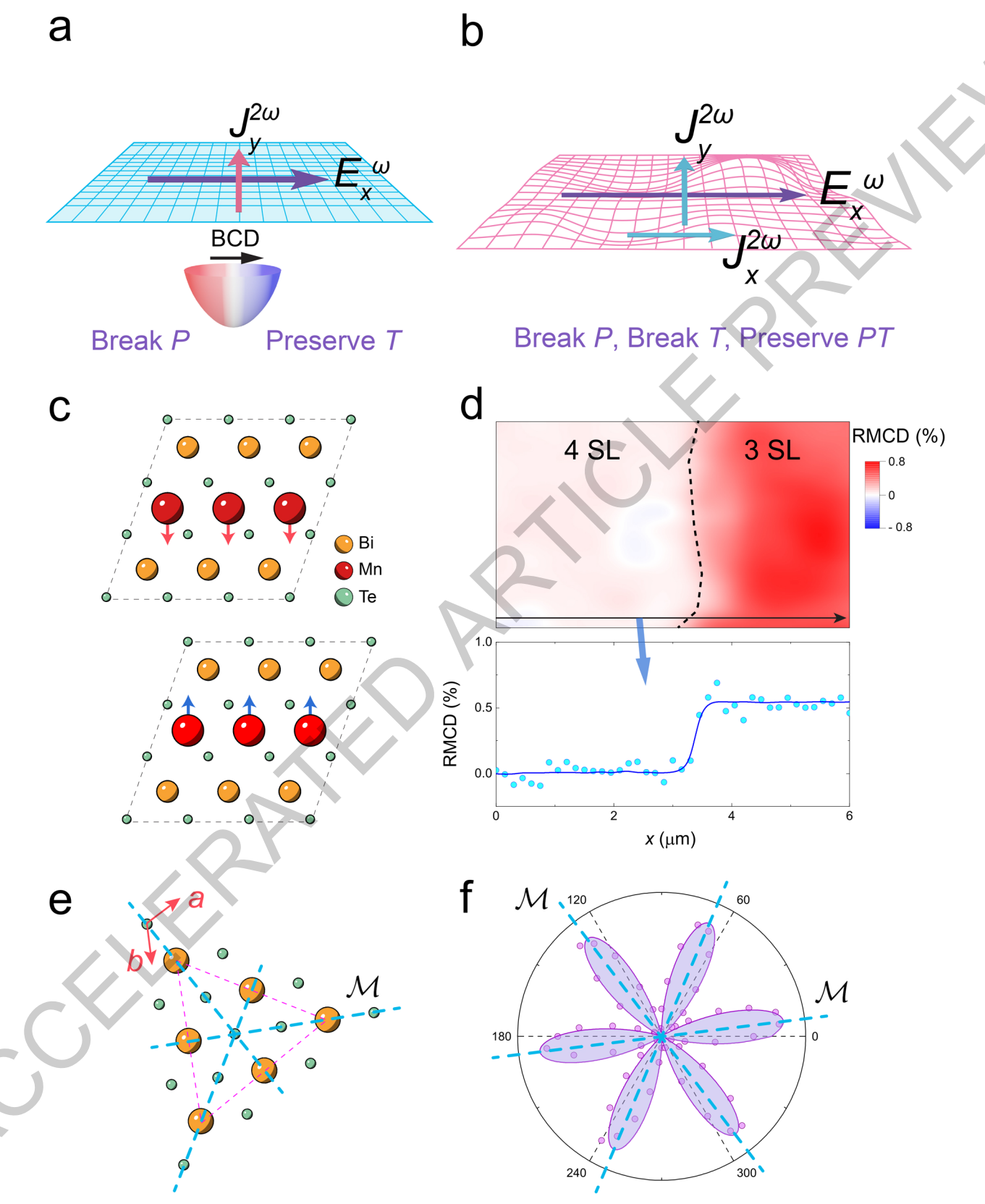

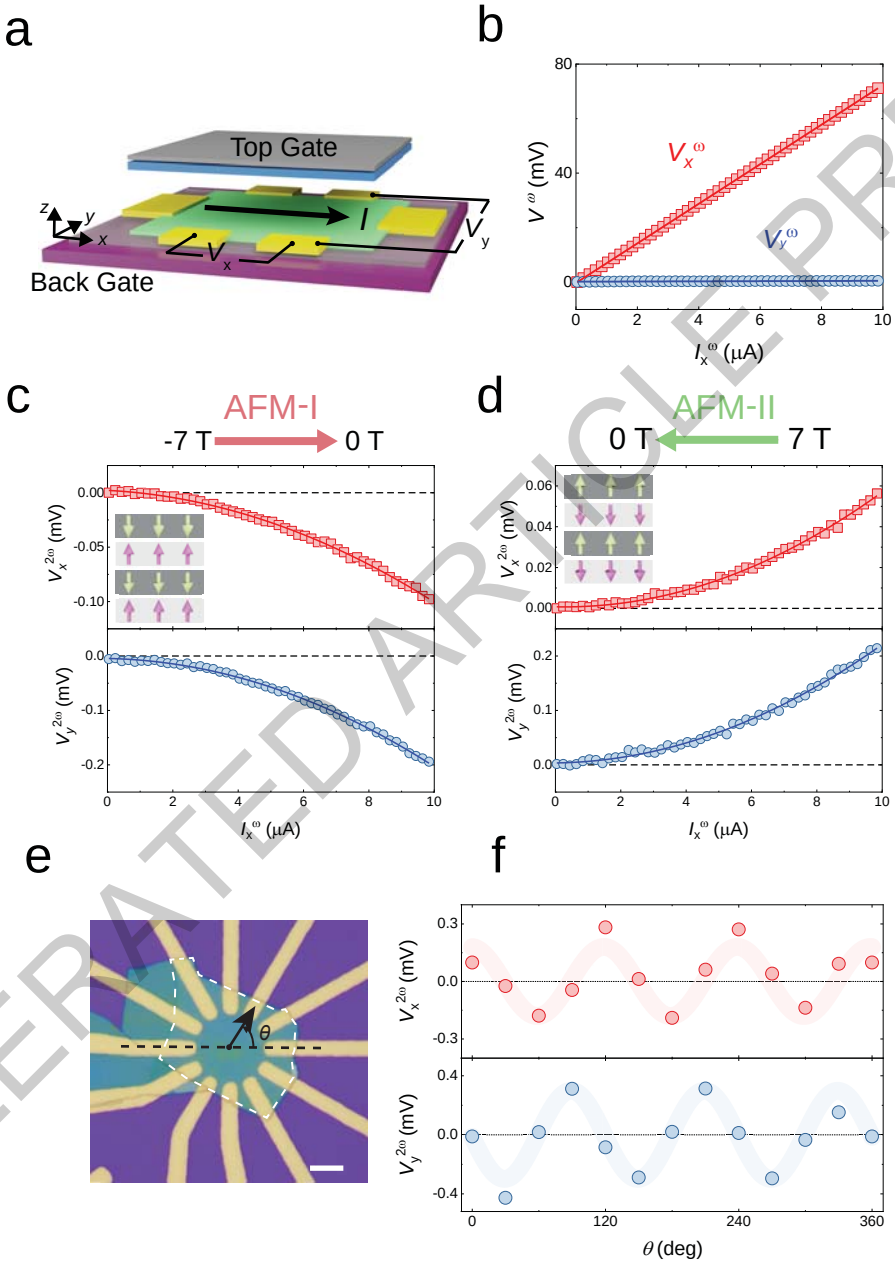

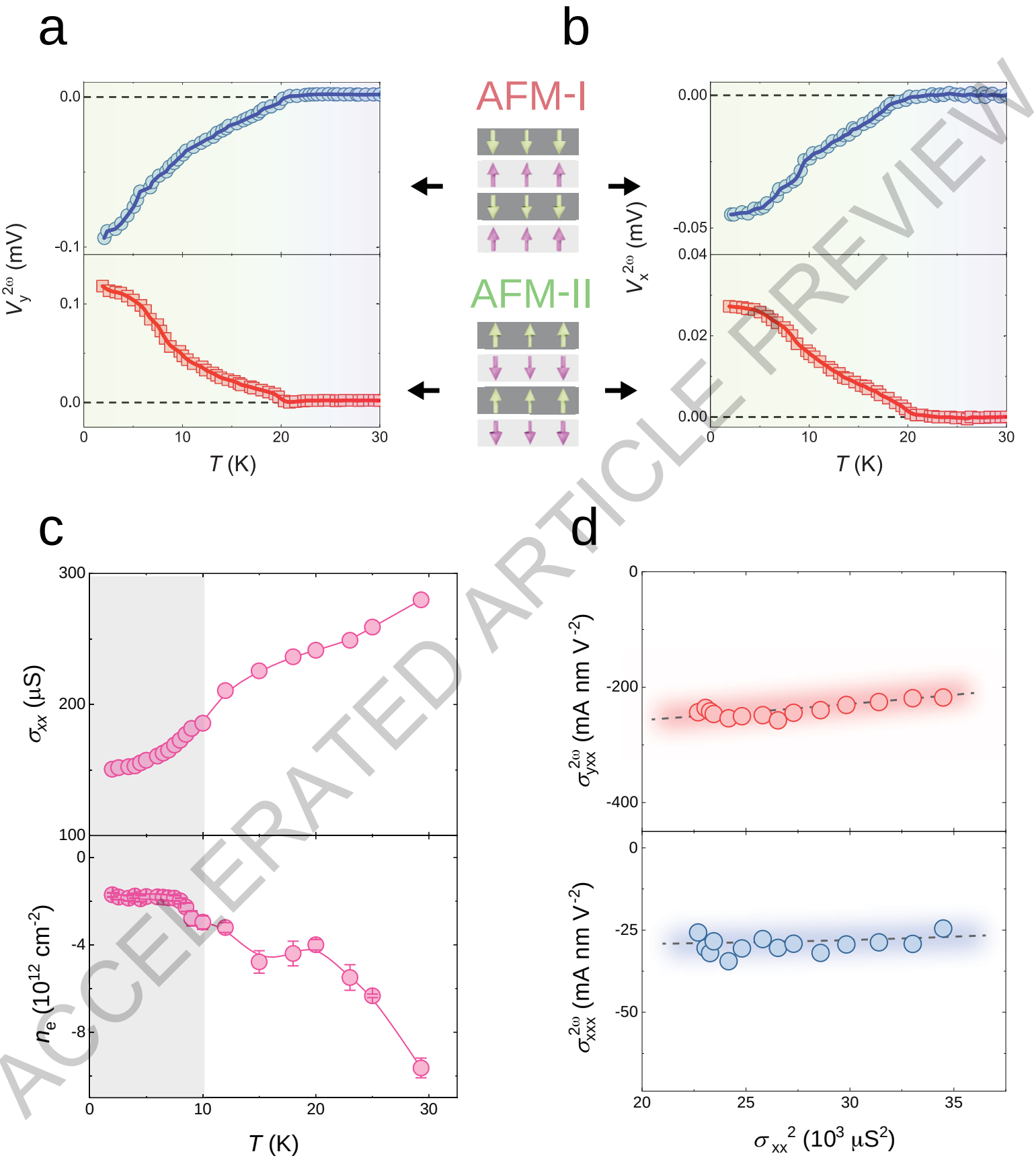

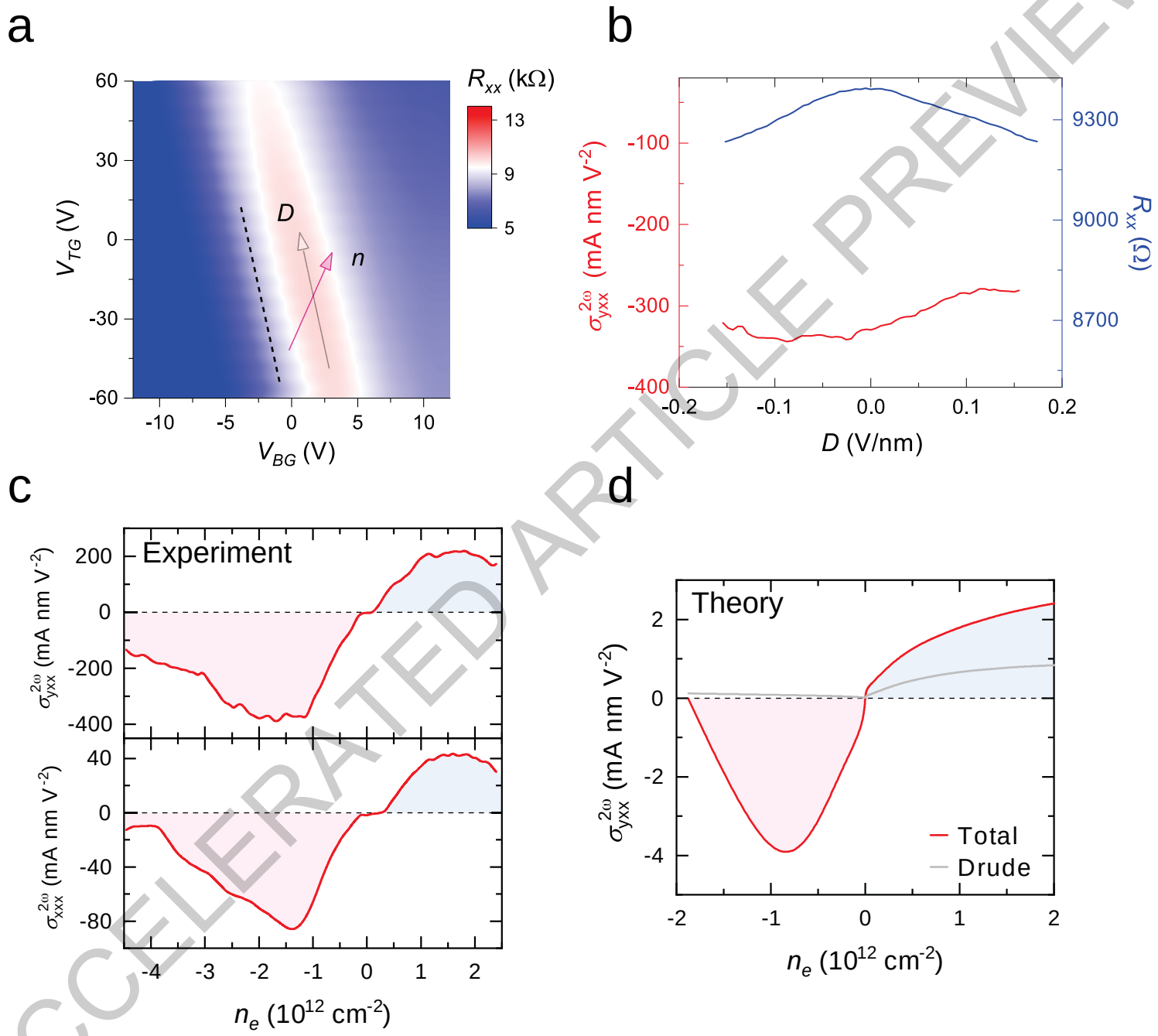

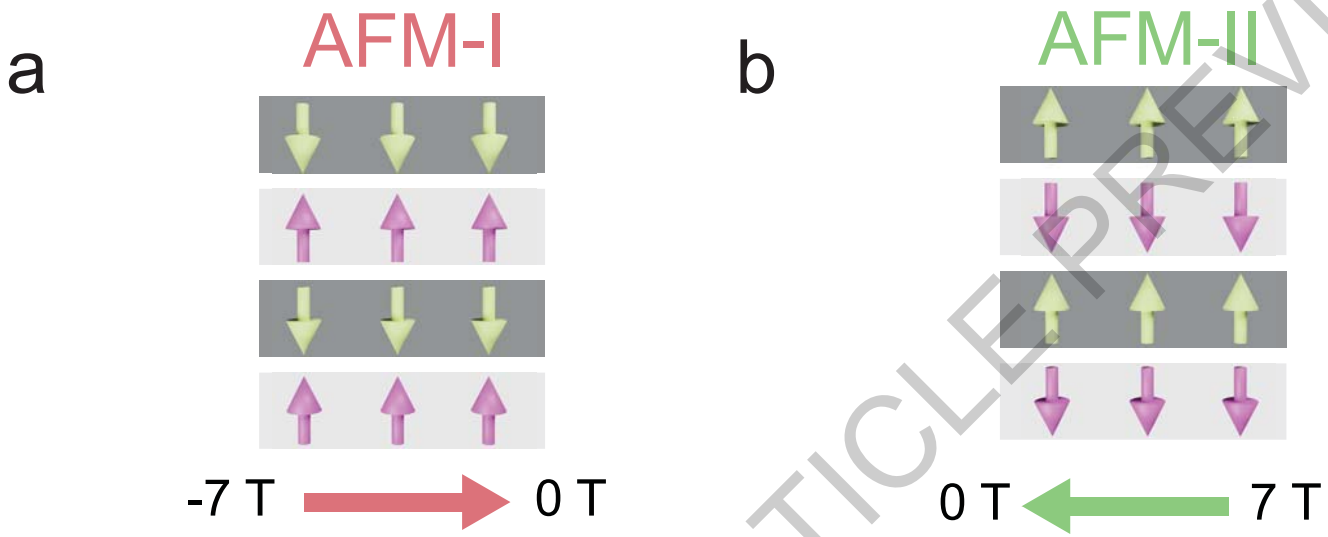

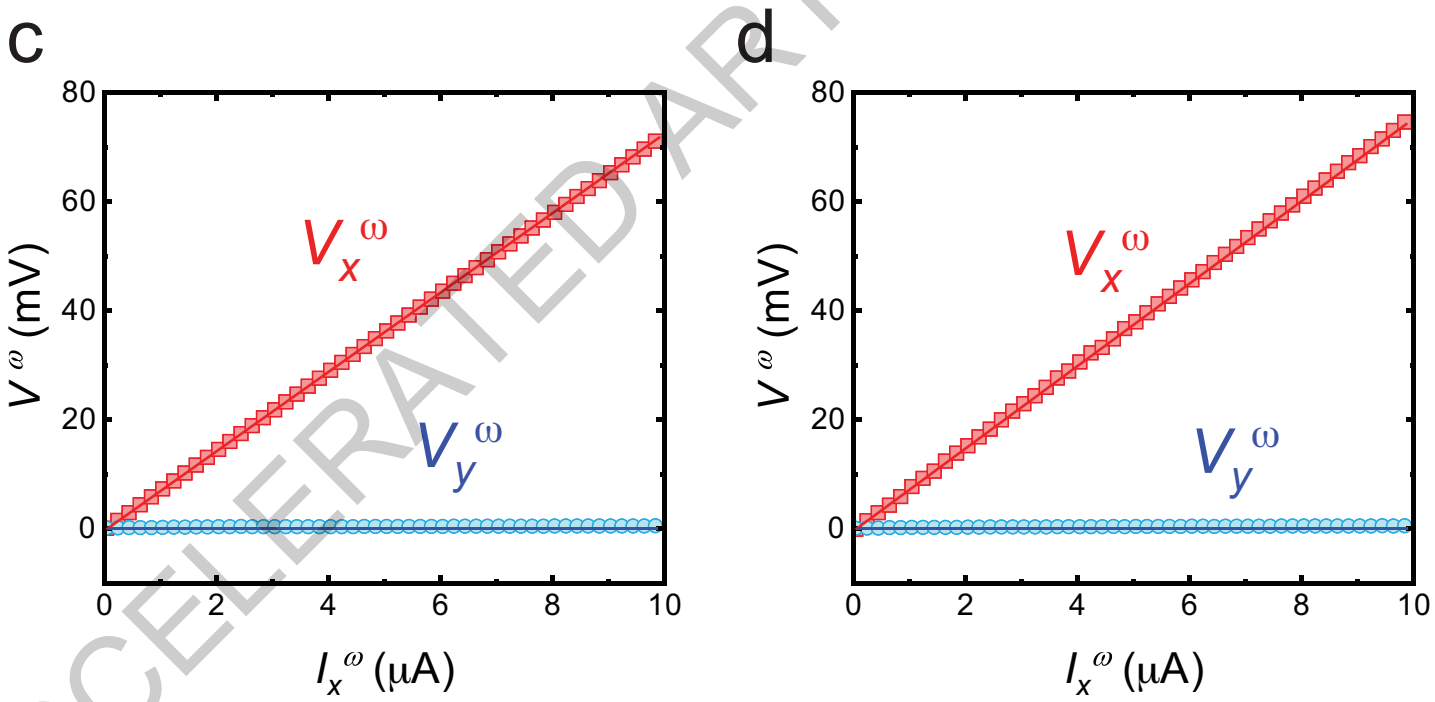

Extended Data Fig. 1

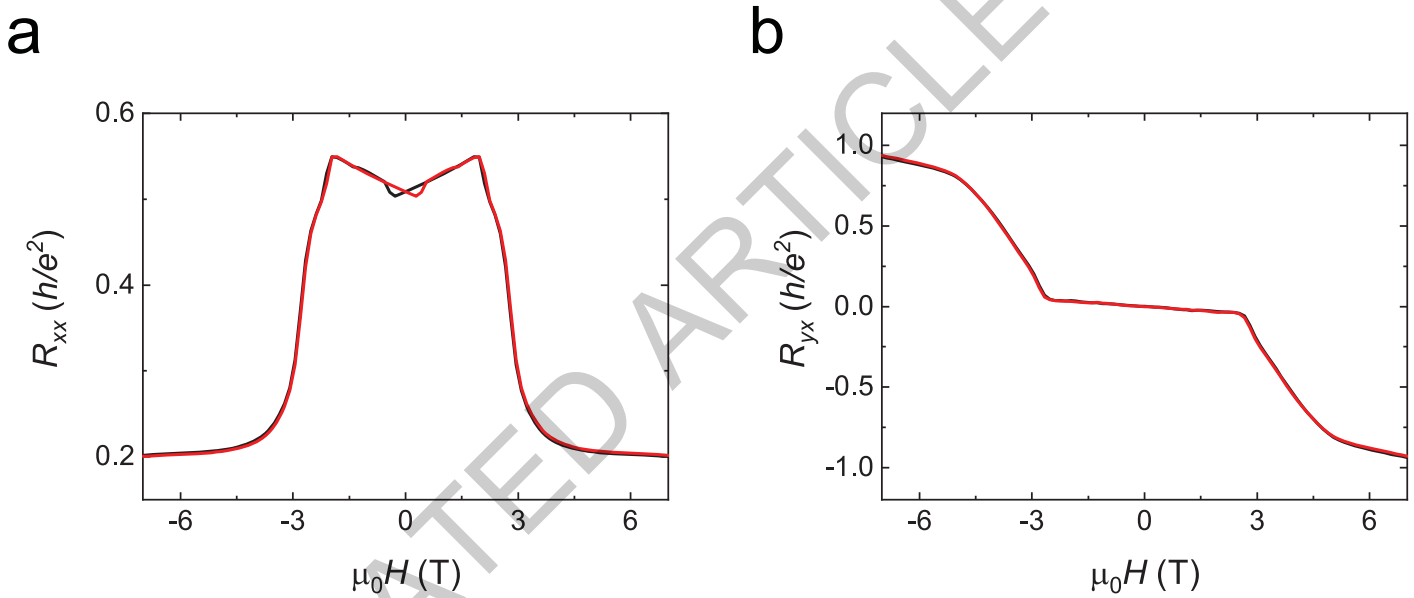

Extended Data Fig. 2

Material	T (K)	$\sigma_{xx}^{1\omega}$(10^{-3}S)	$\sigma_{yxx}^{2\omega}$ (mA nm V^{-2})	Origin
WTe_2 (bilayer)[10]	10	0.15	940	BCD
WTe_2 (few-layer)[9]	2	2.1	3	
Strained WSe_2[13]	140	~ 0.41	~ 1200	
Twisted WSe_2[19]	1.5	~ 0.3	~ 18000	
h-BN/graphene/h-BN[16]	1.7	17.8	1.05×10^7	Skew scattering
$MnBi_2Te_4$ (4-SL)	2	0.15	400	Quantum metric dipole
$MnBi_2Te_4$ (6-SL)	2	0.5	2400	

Extended Data Table 1